Tip-Enhanced Resonance Couplings Revealed by High Vacuum Tip-Enhanced Raman Spectroscopy

Mengtao Sun, Zhenglong Zhang, Li Chen, and Hongxing Xu*

Tip-enhanced resonance couplings (TERCs) are experimentally revealed by high vacuum tip-enhanced Raman spectroscopy (HV-TERS) and theoretically interpreted. The Fermi resonance and Darling–Dennison resonance are successfully observed in HV-TERS, which are the first overtone (or combinational mode)-fundamental interaction (2:1 resonance coupling) and the first overtone-first overtone resonant interaction (1:1 resonance coupling), respectively. The electric field gradient plays an important role on TERCs in HV-TERS at the level of the second-order perturbation theory. The molecular tautomeric effects are also observed from thiourea adsorbed on Ag film in HV-TERS. The reported HERCs can provide a deeper understanding of the importance of molecular anharmonicity in high-order perturbation for TERS. HV-TER spectra provide 'additional' nonlinear Raman peaks, compared with the harmonic zero-order perturbation in HV-TERS, and thus enable ultrasensitive chemical analysis at the nanoscale with more vibrational information.

1. Introduction

Since the discovery of tip-enhanced Raman spectroscopy (TERS) in 2000,[1–3] it has been a prospective spectral tool for chemical analysis[1–14] even at the single molecule level on single crystals,[8–10] because of its high spatial resolution beyond the optical diffraction limit of light and its extremely high optical sensitivity.[1–11] Since a high vacuum system can provide a clean chemical environment for chemical analysis, it is essential to build up TERS in a high vacuum system to achieve a novel solution for chemical analysis.[12–14] To obtain a higher efficiency for the collection of Raman signals, the objective was put into the vacuum chamber and near the tip and the substrate in our novel designed high vacuum TERS (HV-TERS) system[13] (see **Figure 1**). In scanning probe microscopy (SPM)-based TERS, scanning tunneling microscope (STM)-based TERS is the best candidate for simultaneously obtaining the vibration spectral and electronic structural information at the atomic scale at low temperature.

For a molecule placed in an inhomogeneous electromagnetic field, the Hamiltonian for Raman spectra can be written as[15]

$$\begin{aligned} H &= H_0 + H_1 + H_2 \\ &= \alpha_{\alpha\beta} E_\beta E_\alpha + \frac{1}{3} A_{\alpha,\beta\gamma} \frac{\partial E_{\beta\gamma}}{\partial r} E_\alpha \\ &\quad + \frac{1}{3}\left(A_{\gamma,\alpha\beta} E_\gamma + C_{\alpha\beta,\gamma\delta} \frac{\partial E_{\gamma\delta}}{\partial r} \right) \frac{\partial E_{\alpha\beta}}{\partial r} + \cdots \end{aligned} \tag{1}$$

where $\alpha_{\alpha\beta}$, $A_{\alpha\beta\gamma}$, and $C_{\alpha\beta,\gamma\delta}$ are the electric dipole–dipole polarizability, the electric dipole–quadrupole polarizability and the electric quadrupole–quadrupole polarizability, and E_α and $\frac{\partial E_{\alpha,\beta\gamma}}{\partial r}$ are the external electric field and external electric field gradient, respectively. In second-order perturbation theory, the diagonal matrix element contains contributions to harmonic terms and anharmonic terms:

$$\begin{aligned} \langle v_i | H_{vib}^{eff} | v_i \rangle &= \sum_r \omega_r \left(n_r + \frac{1}{2} \right) \\ &\quad + \sum_{r<s} x_{rs} \left(n_r + \frac{1}{2} \right) \left(n_s + \frac{1}{2} \right) + \cdots \end{aligned} \tag{2}$$

where ω_r is the harmonic frequency for mode r, n_r is the vibrational quantum number, and x_{rs} is the anharmonic coupling constant between modes r and s. We restrict our analysis of resonant effects to off-diagonal matrix elements of Fermi resonance[16,17] and Darling-Dennison resonance,[18,19] which can be written as

$$\begin{aligned} &\langle v_r + 1, v_s + 1, v_t | H_{vib}^{eff} | v_r, v_s, v_t + 1 \rangle \\ &= \frac{k_{rst}}{2} \sqrt{\frac{(v_r + 1)(v_s + 1)(v_t + 1)}{2}} \end{aligned} \tag{3}$$

$$\begin{aligned} &\langle v_r + 2, v_t | H_{vib}^{eff} | v_r, v_t + 1 \rangle \\ &= \frac{k_{rrt}}{4} \sqrt{\frac{(v_r + 2)(v_r + 1)(v_t + 1)}{2}} \end{aligned} \tag{4}$$

$$\begin{aligned} &\langle v_r + 2, v_t | H_{vib}^{eff} | v_r, v_t + 2 \rangle \\ &= \frac{k_{rrtt}}{4} \sqrt{(v_r + 1)(v_r + 2)(v_t + 1)(v_t + 2)} \end{aligned} \tag{5}$$

Equations (3) and (4) are the Fermi resonances for the combinational and overtone modes, respectively, and (5) is the

Prof. M. Sun, Dr. Z. Zhang, Dr. L. Chen, Prof. H. Xu
Beijing National Laboratory
for Condensed Matter Physics
Institute of Physics
Chinese Academy of Sciences
PO Box 603–146, Beijing, 100190, PR China
E-mail: mtsun@aphy.iphy.ac.cn
Prof. H. Xu
School of Physics & Technology
Wuhan University
Wuhan, 430072, PR China

DOI: 10.1002/adom.201200074

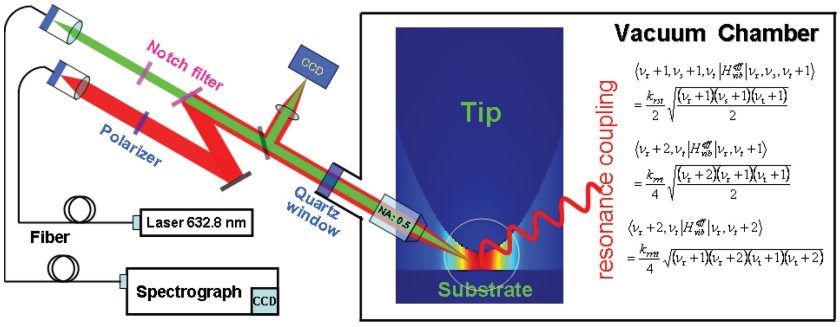

Figure 1. (a) The home-made HV-TERS, and the tip-enhanced resonance coupling.

In this paper, using the advantages of TERS, we report the experimental discovery of TERCs in HV-TERS. The tip-enhanced Fermi resonance, Darling–Dennison resonance, molecular tautomeric effect, and resonances related to the tautomeric effect are successfully experimentally observed and rationally interpreted theoretically. Our experimental studies reveal the importance of TERCs in HV-TERS, which provides much more convincing ultrasensitive vibrational information for chemical analysis.

Darling-Dennison resonance for first overtone modes, where k_{rst}, k_{rrt}, and k_{rrtt} are anharmonic force constants. Their operators in Equations (3)–(5) can be written as[20]

$$V_{rst(rrt)}^{Fermi} = k_{rst(rrt)} a_r^+ a_{s(r)} a_t + \text{Hermitian conjugate} \quad (6)$$

$$V_{rrtt}^{DD} = k_{rrtt} a_r^+ a_r^+ a_t a_t + \text{Hermitian conjugate} \quad (7)$$

In Equations (6), (7) a^+ and a are the raising and lowering operators.

Until now, almost all the studies on TERS have mainly focused on the diagonal part in Equation (1) and on the configuration of the molecule adsorbed on the substrate, while tip-enhanced resonance couplings (TERC), experimentally and theoretically, remain to be explored in HV-TERS. For example, unexpected 'additional' Raman peaks appearing in TER spectra can be attributed to molecular anharmonicity, which can provide abundant vibrational information for chemical analysis. Fermi resonance[16,17] and Darling–Dennison resonance[18,19] are expected to play the most important roles in TERCs (see Figure 1).

Many molecules have tautomeric forms, e.g., thiourea occurs in two tautomeric forms (see **Figure 2**). Theoretical calculations revealed that they will stand on the substrates by adsorption, and the interaction between the thione form and Ag is stronger. In aqueous solution, the thione form shown predominates. To our best knowledge, the molecular tautomeric effect and Fermi resonance as well as Darling-Dennison resonance, related to the molecular tautomeric effect, have not been simultaneously reported in HV-TERS.

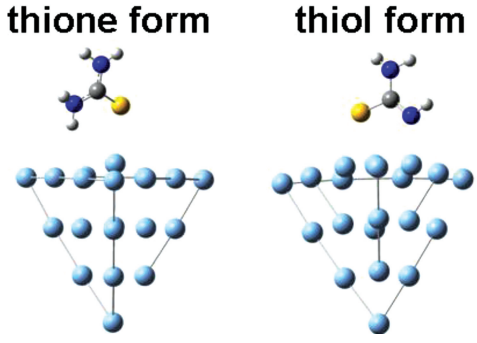

Figure 2. Chemical structures of thiourea in thione (a) and thiol (b) forms adsorbed on Ag_{20} cluster, respectively.

2. Results and Discussion

2.1. Wavelength-Scanning Surface Plasmon Resonance in HV-TERS

To realize the maximal local surface plasmon resonance (LSPR) in the nanogap of HV-TERS, wavelength-scanning SPRs were calculated, considering different tip size and nanogap distances. **Figure 3**a is the model used in calculations, where θ is the angle between the tip and incident light, d is the distance between tip and substrate, R is the radius of tip, and the tip and the substrate are Au and Ag, respectively. Figure 3b reveals the wavelength-scanning SPRs at different values of d, and the radius of the tip size R = 30 nm. It is found that there are two distinct strong LSPRs around 620 and 860 nm, and the intensity of these two peaks increases significantly with decreasing d, while their shifts are minimal. In atomic force microscopy (AFM)-based TERS, the nanogap is usually 2 nm; while in scanning tip microscopy (STM)-based TERS, the nanogap can be manipulated within 1 nm by the tunneling current and bias voltage. Around 632.8 nm, Figure 3b reveals that plasmon intensity ($|E|^2$) of STM-TERS can reach up to ~4×10^7, while that of AFM-TERS is only ~1×10^6. This is one of the advantages of STM-TERS as compared to AFM-TERS. Figures 3c,d reveal that with the increase of d, these two plasmon peaks are significantly decreased, but the plasmon peak at high energy decreases much more quickly than that at low energy. When the nanogap is large enough (d = 50 nm), these two plasmon peaks are almost merged into one plasmon peak (see Figure 3d). This phenomenon reveals that these two plasmon peaks in Figure 3b are caused by the strong coupling between tip and substrate, which can be interpreted by the hybrid plasmonic structure[21] of TERS (see Figure 3e), and the energy difference Δ increases with decreasing d (the stronger coupling between tip and substrate results in a larger separation between these two SPR peaks in Figure 3c,d).

Figure 3f shows the wavelength-scanning SPRs with different R of tip, where d = 2 nm. It is found that with an increase in R, the plasmon peaks around 620 nm are slightly blueshifted and the intensity of the SPRs are also slightly increased; the second peaks around 860 nm are not shifted, but the intensity of the SPRs are strongly decreased. The blueshift of the plasmon peak around 620 nm may result from the increased energy difference Δ shown in Figure 3e with the increase of tip

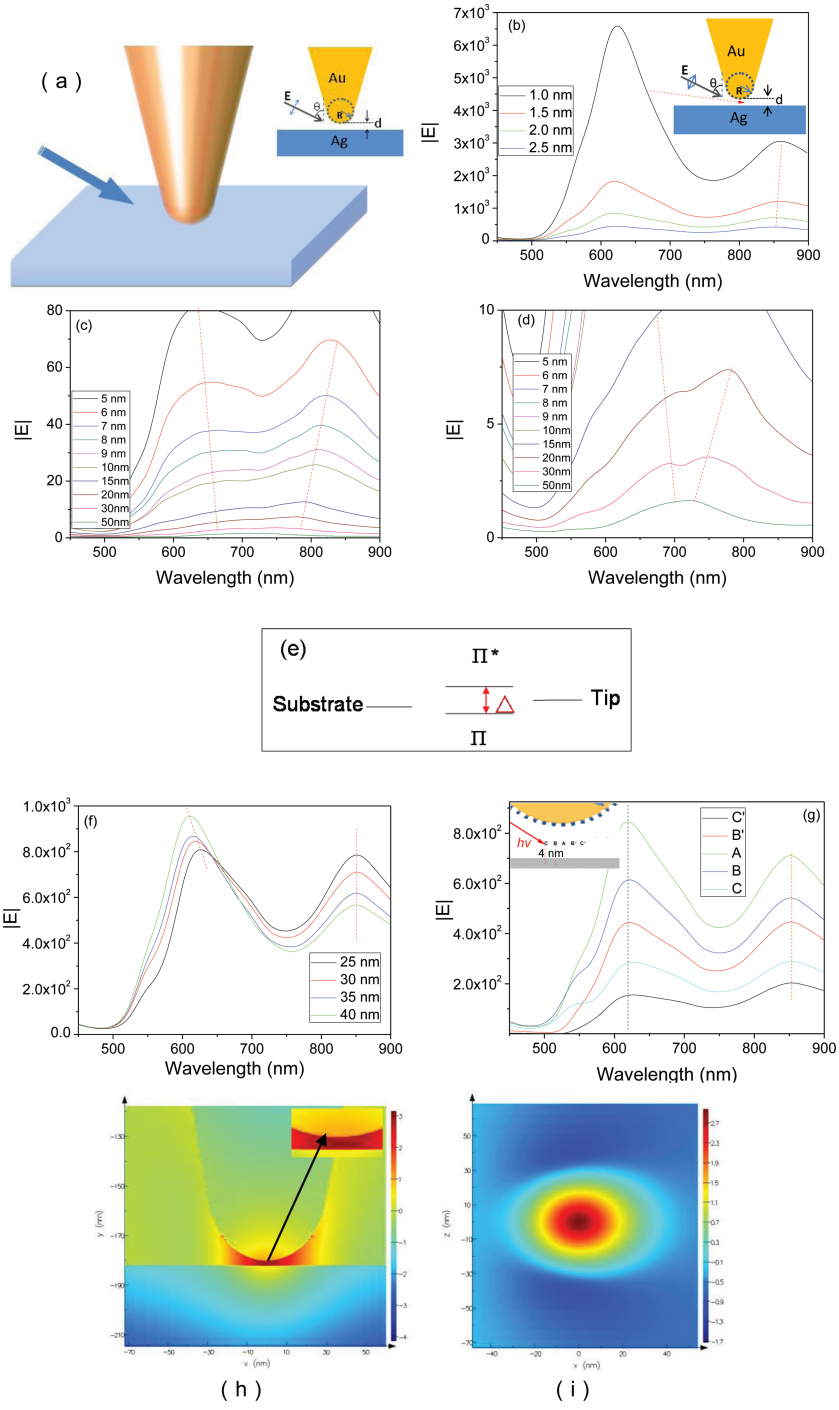

Figure 3. (a) The model of TERS; (b–d) distance-dependent wavelength-scanning SPRs; (e) hybrid plasmonic model of TERS; (f) tip size-dependent wavenumber-scanning SPRs; (g) site-dependent SPRs; (h,i) electric field distribution (in log scale) along the tip and along the substrate, respectively.

size in TERS, where the hybrid is increased with the increase in the tip size.

To study the site-dependent wavelength-scanning SPR (see Figure 3g), we choose five different sites (see inset Figure 3g). It is found that the profiles of all are the almost same, but the intensities of SPRs are asymmetric, where the intensity at the site of the incoming laser is stronger than that at the back side of this point. In Equation (1), electric field and electric field gradient are included. The calculated electric field intensity along the tip and along the surface above the substrate in the center of the nanogap can be seen from Figure 3h,i, where $d = 2$ nm and $R = 30$ nm. It was found that the intensity of the electric field gradient along the surface above the substrate is significantly larger than that along the tip, due to the strongly asymmetric distribution along the substrate.

2.2. Darling–Dennison Resonance

Figure 4a is the HV-TER spectrum of thiourea adsorbed on Ag film in the region from 800 to 1050 cm^{-1}, where five Raman peaks are found. To interpret these five Raman peaks, we measured a normal Raman scattering (NRS) spectrum of thiourea powder (Figure 4b), which revealed that there is no Raman peak in this region. These five Raman peaks in Figure 4a are therefore not from the vibrational modes at the fundamental frequency. Since the thione form of thiourea is dominant in aqueous solution,[19] and thiourea adsorbed on Ag_{20} cluster in the thione form is more stable, the measured peaks should be mainly from thiourea in the thione form. So, theoretical simulations of thiourea (in thione form) adsorbed on Ag_{20} cluster is used to interpret Figure 4a. It is revealed that there is not any normal mode in the region from 800 to 1050 cm^{-1} (see Figure 4c). Note that there are no Raman peaks in 600–700 cm^{-1} in the measured normal Raman spectrum in Figure 4b, while there are two weak peaks in the simulated Raman spectrum of the molecule adsorbed on the Ag metal in Figure 4c. The reason is that these two peaks are too weak to be observed in a normal Raman spectrum, but the interaction between the molecule and the metal results in an enhancement of these two vibrational modes (modes 'e' and 'f' in Figure 4c). The vibrational modes 'e' and 'f' and the interaction between molecule and metal can be seen in Figure 4e.

Tip-enhanced Darling–Dennison resonance can interprete four of the five peaks. Peaks 'A' and 'B' in Figure 4a are two perturbed (resonant interaction) first overtone modes, and their perturbed foundational modes 'a' and 'b' can be seen in Figure 4c. Peaks 'C' and 'D' in Figure 4a are two perturbed (resonant interaction) first overtone modes, and their perturbed foundational modes 'c' and 'd' can be seen in

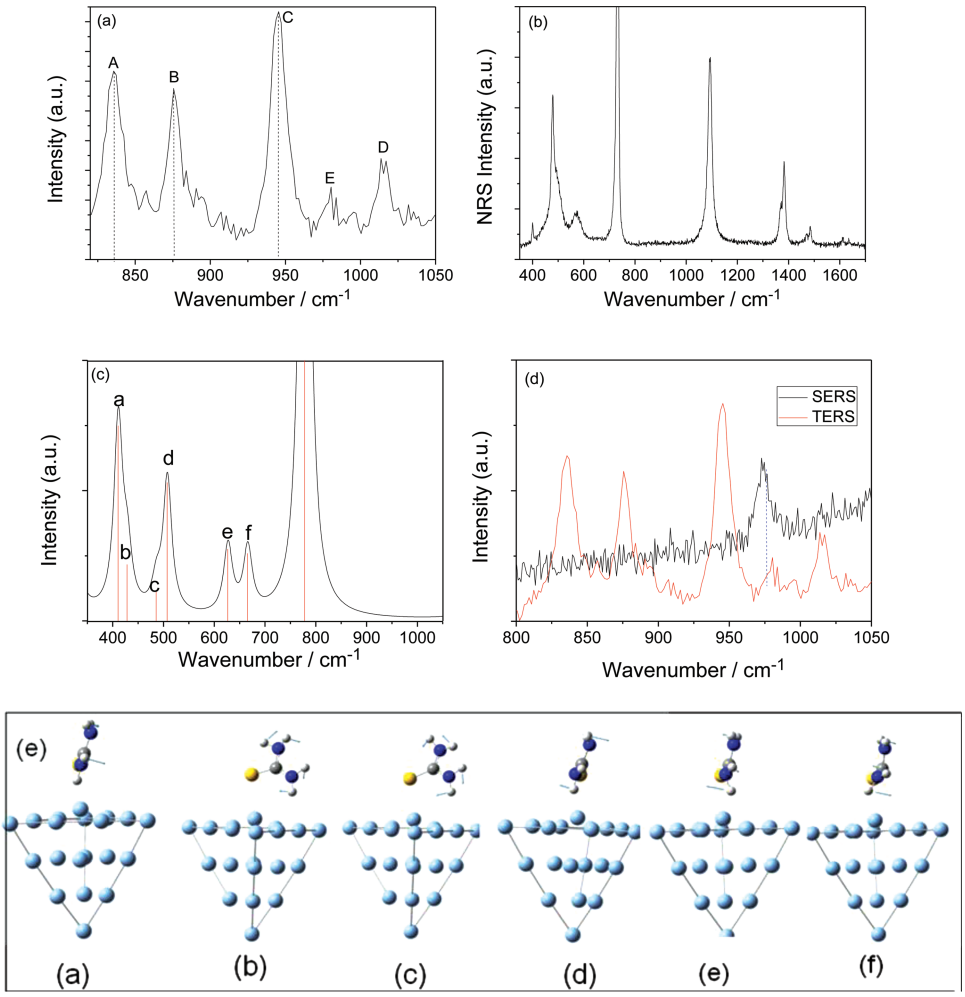

Figure 4. (a) TER spectrum in the region from 800 to 1050 cm^{-1}, (b) the measured normal Raman spectrum of thiourea powder, (c) the simulated Raman spectrum of thiourea adsorbed on Ag_{20} cluster in thione form, (d) the measured SERS and TER spectra in the region from 800 to 1050 cm^{-1}, and (e) the calculated vibrational modes.

Figure 4c. Note that without the tip in SERS (see Figure 4d), Darling–Dennison resonance can not be observed experimentally. The peak 'E' in Figure 4a should be the combinational modes of 'c' and 'd'. To confirm this, we also measured the SERS of thiourea on Ag film, and it was found that this peak can also be found in Figure 4d. The slight shift for peak 'E' between SERS and TERS results from the influence of the tip. In SERS, without the help of TER spectra, peak 'E' is hard to interpret with combinational modes, since there is neither the perturbed fundamental peak for Fermi resonance, nor the perturbed overtone mode for Darling–Dennison resonance (the Darling–Dennison resonance is too weak to be observed in SERS). The vibrational modes can be seen in Figure 4e.

2.3. The Tautomeric Effect and Fermi Resonance

TER spectra revealed that there are four strong Raman peaks from 1400 to 1700 cm^{-1} (see **Figure 5**a), but the simulated Raman spectrum of thiourea in thione form revealed that there are only two Raman peaks. One has to consider the Raman spectrum of thiourea in thiol form. It is found that the Raman spectrum of thiourea in thiol form can help interprete the above phenomenon. In Figure 5a, the Raman peaks 'K' and 'L' are the symmetric and asymmetric modes of thione form, respectively, and Raman peak 'J' of the thiol form is similar to the vibrational mode 'K' of the thione form. The Raman peak 'M' in Figure 5a,b can be interpreted as Fermi-like resonance, which is the combinational modes 'g' and 'h' in the thiol form (see Figure 5c), while the perturbed fundamental peak 'K' is from thiourea in the form of thione. We called the tautometric effect-related Fermi-like resonance Sun-Fermi resonance. The Raman modes of this can be seen in Figure 5d.

2.4. Other Nonlinear Resonances in TER Spectra

While there are many more Raman peaks in experimental TER spectra from 1100 cm^{-1} to 1350 cm^{-1} in **Figure 6**a, the intensities of these Raman peaks were much weaker than those in

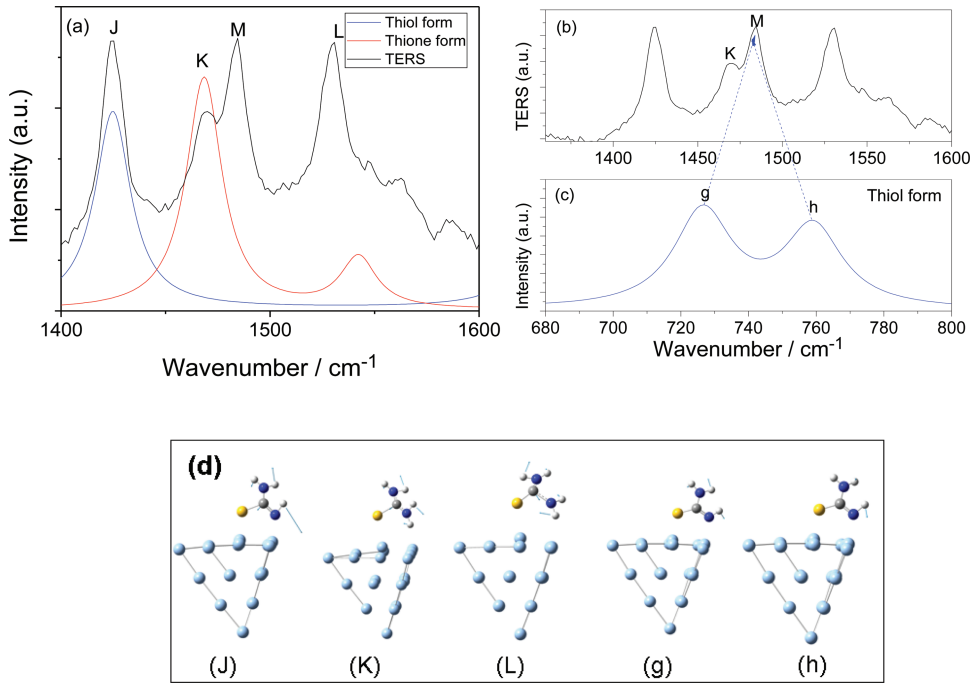

Figure 5. (a–c) The experimental TER spectrum and simulated Raman spectra of thiourea in thione and thiol forms, and (d) the calculated vibrational modes.

other regions (see Figure S1 in the Supporting Information). The Raman peak at 1127 cm^{-1} in Figure 6a,b is the fundamental mode of thiourea in thione form. Figure 6b,c shows the theoretical interpretation of the mechanism of these additional peaks. Figure 6d reveals that there are two degenerate vibrational modes at 1127 cm^{-1}. To interpret these 'additional' peaks, we firstly study the influence of overtone (or combinational) modes. In this region, tip-enhanced Darling–Dennison-like

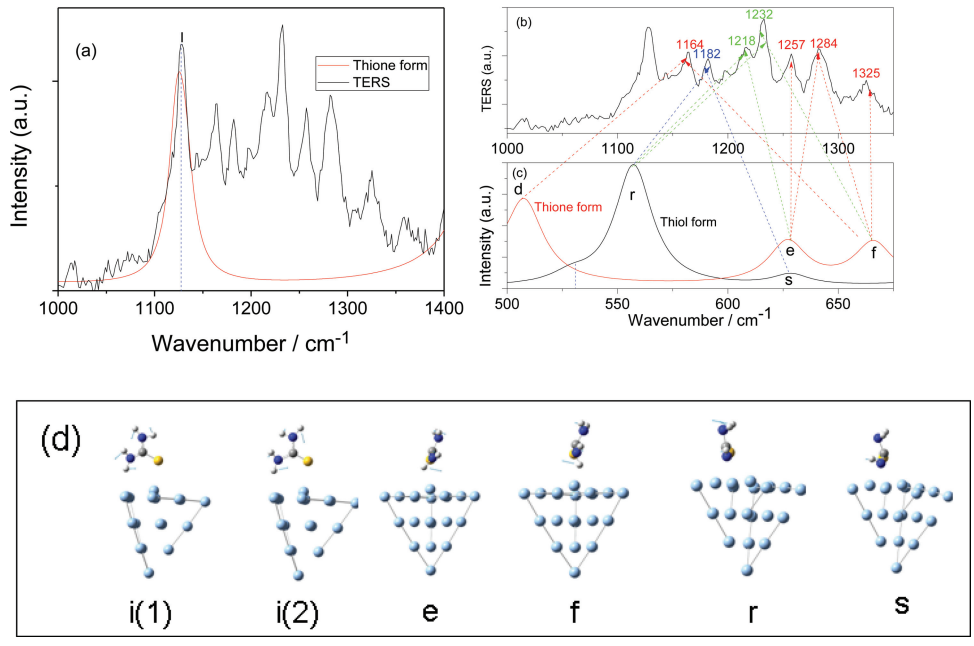

Figure 6. (a) TER spectrum and simulated Raman spectrum, (b,c) the mechanisms of different resonance couplings, and (d) the calculated vibrational modes.

resonances were also observed experimentally in HV-TER spectra. The Raman peaks at 1164 and 1182 cm^{-1} are the combinational modes of thione and thiol forms, respectively, and these two combinational modes are resonantly coupled and gaining strong Raman intensities. These two combinational modes from two tautomeric forms at the level of combinational mode, are called Sun-Zhang resonance. The Raman peaks at 1218 and 1232 cm^{-1} are the combinational modes, where their fundamental frequencies are from thione and thiol form for each combinational mode, respectively. These two combinational modes from two tautomeric forms at the level of fundamental modes are called Sun-Xu resonance. All of their vibrational modes can be seen in Figure 6d.

The Raman peaks at 1257 and 1325 cm^{-1} are the first overtone modes of 623 and 662 cm^{-1}, respectively, and their first overtone–overtone resonance coupling result in Darling–Dennison resonance. The Raman peak at 1284 cm^{-1} is the combinational modes of 623 and 662 cm^{-1}. The combinational modes at 1284 cm^{-1} in Figure 6b and 975 cm^{-1} in Figure 6a were resonantly coupled with the first overtone modes of Darling–Dennison resonance. All of their vibrational modes can be seen in Figure 6d.

2.5. The Relationship Between Theoretical Calculations and Experimental Results

To obtain the best experimental measurement in TERS, the strongest plasmon resonance in Equation (1) is needed around an incident light of 632.8 nm. Figures 3b–d demonstrate that there is a strong surface plasmon resonance around 632.8 nm. To obtain the strong nonlinear Raman (such as the appearance of the Fermi resonance or Darling–Dennison resonance) in TERS, the higher order terms in Equation (1) should be large enough, which require strong intensities of the electric field and the electric field gradient, and their strong coupling. Figures 3h,j revealed that there is a strong electric field intensity and electric field gradient around an incident light of 632.8 nm. The strong coupling between the strong electric field and strong electric field gradient results in the experimental observations of Fermi resonances and Darling–Dennison resonances shown in Figures 4, 5, 6. Note that there are always strong electric fields and strong electric field gradients in the distance of a nanogap from 1 to 2 nm in HV-TERS, which were demonstrated by the calculated results in Figures 3b–d.

Note that TERCs were observed experimentally from HV-TER spectra. The influence of HV to TERCs in TERS under ambient conditions is an interesting issue for future experimental investigation,[22] though theoretical calculations have revealed that the coupling between tip and substrate is the most important factor for the observation of TERCs in TERS.

3. Conclusion

TERCs, including Fermi resonance and Darling–Dennison resonance, the tautomeric effect, and tautomeric-related resonance couplings were experimentally observed in HV-TERS and rationally interpreted theoretically. These tip-enhanced anharmonic Raman spectra can be well used to interpret the 'additional' Raman peaks in linear harmonic TERS. The electric field gradient plays an important role on TERCs in HV-TERS at the level of the second-order perturbation theory. These abundant Raman peaks can provide much more convincing vibrational information for chemical analysis. Their correct understanding can significantly promote applications of TERS in ultrasensitive spectral analysis at the nanoscale.

4. Experimental Section

TER spectra were measured with a home-built HV-TERS setup (see Figure 1). It consists of a home-built scanning tunneling microscope (STM) in a high vacuum chamber, a Raman spectrometer with a 100 μW 632.8 nm He-Ne laser incidents at 60° to the tip axis, and piezo stages for 3D tip and sample manipulations. The long working distance objective (NA = 0.5) was placed in the high vacuum chamber with a pressure of 10^{-7} Pa. The holographic grating (1800 grooves/mm) and the slit lead to a spectra resolution of 1 cm^{-1}. The tunneling current and bias voltage are 1 nA and 1 V, respectively. A gold tip with a diameter of about 50 nm was made by electrochemical etching of a 0.25 mm diameter gold wire.[23] The substrate was prepared by evaporating a 100 nm silver film onto a newly cleaned mica film under high vacuum. The film was immersed in a 1×10^{-5} M thiourea in ethanol solution for 24 h, and then washed with ethanol for 10 min to guarantee that there was only one monolayer of molecules adsorbed on the silver film. Then the sample was immediately put into the high vacuum chamber. To get a good signal-to-noise ratio, the TERS signals were collected with an acquisition time of 10 s and accumulated 5 times for each spectrum. We also measured normal Raman scattering spectra of thiourea powder, and ambient SERS of thiourea adsorbed on Ag film at the concentration of 10^{-5} M, using Leica microscopy equipment in a confocal Raman spectroscopic system (Renishaw, Invia), and the incident wavelength is 632.8 nm.

The wavelength-scanning SPRs and electric field distribution were calculated, using the finite difference time domain (FDTD) method,[24] which is implemented in FDTD Solutions.[25] the model in the calculations can be seen in Figure 3a. The permittivity of Au and Ag was taken from the work edited by Palik.[26] Theoretical simulations of Raman spectra were done with density functional theory,[27] B3LYP functional,[28] 6–31G(d) basis for S, C, and N, LANL2DZ basis[29] for Ag. The cluster of Ag_{20} tetrahedron[30] is used for the metal substrate. All of quantum chemical calculations were done with Gaussian 09 software.[31]

Supporting Information

Supporting Information is available from the Wiley Online Library or from the author.

Acknowledgements

This work was supported by the National Basic Research Project of China (Grants 2009CB930701), the National Natural Science Foundation of China (Grants 90923003, 10874234 and 20703064) and the Program of Shenyang Key Laboratory of Optoelectronic materials and technology (Grant No. F12–254–1–00).

Received: December 29, 2012
Revised: March 18, 2013
Published online: April 25, 2013

[1] R. M. Stockle, Y. D. Suh, V. Deckert, R. Zenobi, *Chem. Phys. Lett.* **2000**, *318*, 131.
[2] M. S. Anderson, *Appl. Phys. Lett.* **2000**, *76*, 3130.
[3] N. Hayazawa, Y. Inouye, Z. Sekkat, S. Kawata, *Opt. Commun.* **2000**, *183*, 333.
[4] B. Pettinger, P. Schambach, C. J. Villagomez, N. Scott, *Annu. Rev. Phys. Chem.* **2012**, *63*, 379.
[5] J. Stadler, T. Schmid, R. Zenobi, *Nanoscale* **2012**, *4*, 1856.
[6] E. Bailo, V. Deckert, *Chem. Soc. Rev.* **2008**, *37*, 921.
[7] A. Hartschuh, *Angew. Chem., Int. Ed.* **2008**, *47*, 2.
[8] Z. Yang, Q. Li, Y. Fang, M. Sun, *Chem. Commun.* **2011**, *47*, 9131.
[9] K. F. Domke, D. Zhang, B. Pettinger, *J. Am. Chem. Soc.* **2006**, *128*, 14721.
[10] J. Steidtner, B. Pettinger, *Phys. Rev. Lett.* **2008**, *100*, 236101.
[11] M. D. Sonntag, J. M. Klingsporn, L. K. Garibay, J. M. Roberts, J. A. Dieringer, T. Seideman, K. A. Scheidt, L. Jensen, G. C. Schatz, R. P. Van Duyne, *J. Phys. Chem. C* **2012**, *116*, 478.
[12] J. Steidtner, B. Pettinger, *Rev. Sci. Instrum.* **2007**, *78*, 103104.
[13] M. T. Sun, Z. L. Zhang, H. R. Zheng, H. X. Xu, *Sci. Rep.* **2012**, *2*, 647.
[14] N. Jiang, E. T. Foley, J. M. Klingsporn, M. D. Sonntag, N. A. Valley, J. A. Dieringer, T. Seideman, G. C. Schatz, M. C. Hersam, R. P. Van Duyne, *Nano Lett.* **2012**, *12*, 5061.
[15] A. D. Buckingham, *Adv. Chem. Phys.* **1967**, *12*, 107.
[16] E. Fermi, *Z. Phys.* **1931**, *71*, 250.
[17] M. T. Sun, Y. R. Fang, Z. Y. Zhang, H. X. Xu, *Phys. Rev. E* **2013**, *87*, 020401(R).
[18] B. T. Darling, D. M. Dennison, *Phys. Rev.* **1940**, *57*, 128.
[19] Y. Q. Li, P. J. Wang, Z. L. Zhang, Y. Z. Li, F. C. Ma, M. T. Sun, *RSC Adv.* **2012**, *2*, 12160.
[20] M. E. Kellman, *Annu. Rev. Phys. Chem.* **1995**, *46*, 395.
[21] E. Prodan, C. Radloff, N. J. Halas, P. Nordlander, *Science* **2003**, *302*, 419.
[22] Our home-made TERS works well in high vacuum. It is difficult to perform the investigation on TERCs from TER spectra at ambient conditions because of two reasons: Firstly, the high vacuum is difficult to recover well once it has been adjusted to ambient conditions. Secondly, we are afraid that our home-made HV-TERS would be damaged in these processes.
[23] B. Ren, G. Picardi, B. Pettinger, *Rev. Sci. Instrum.* **2004**, *75*, 837.
[24] K. S. Kunz, R. J. Luebber, *The Finite Difference Time Domain Method for Electromagnetics*, CRC Press, Cleveland, OH **1993**.
[25] FDTD Solutions, version 7.5, Lumerical Solutions, Inc., Vancouver, BC, Canada **2011**.
[26] *Handbook of Optical Constants of Solids* (Ed: E. D. Palik), Academic Press, New York **1985**.
[27] R. M. Dreizler, E. K. U. Gross, *Density Functional Theory, an Approach to the Quantum Many-Body Problem*, Springer-Verlag, Berlin **1990**.
[28] J. P. Perdew, K. Burke, Y. Wang, *Phys. Rev. B* **1996**, *54*, 16533.
[29] P. J. Hay, W. R. Wadt, *J. Chem. Phys.* **1985**, *82*, 270.
[30] M. T. Sun, S. S. Liu, M. D. Chen, H. X. Xu, *J. Raman Spectrosc.* **2009**, *40*, 137.
[31] M. J. Frisch, G. W. Trucks, H. B. Schlegel, G. E. Scuseria, M. A. Robb, J. R. Cheeseman, G. Scalmani, V. Barone, B. Mennucci, G. A. Petersson, H. Nakatsuji, M. Caricato, X. Li, H. P. Hratchian, A. F. Izmaylov, J. Bloino, G. Zheng, J. L. Sonnenberg, M. Hada, M. Ehara, K. Toyota, R. Fukuda, J. Hasegawa, M. Ishida, T. Nakajima, Y. Honda, O. Kitao, H. Nakai, T. Vreven, J. A. Montgomery Jr., J. E. Peralta, F. Ogliaro, M. Bearpark, J. J. Heyd, E. Brothers, K. N. Kudin, V. N. Staroverov, R. Kobayashi, J. Normand, K. Raghavachari, A. Rendell, J. C. Burant, S. S. Iyengar, J. Tomasi, M. Cossi, N. Rega, J. M. Millam, M. Klene, J. E. Knox, J. B. Cross, V. Bakken, C. Adamo, J. Jaramillo, R. Gomperts, R. E. Stratmann, O. Yazyev, A. J. Austin, R. Cammi, C. Pomelli, J. W. Ochterski, R. L. Martin, K. Morokuma, V. G. Zakrzewski, G. A. Voth, P. Salvador, J. J. Dannenberg, S. Dapprich, A. D. Daniels, O. Farkas, J. B. Foresman, J. V. Ortiz, J. Cioslowski, D. J. Fox, *Gaussian 09*, Revision A.02, Gaussian, Inc., Wallingford, CT, **2009**.